J Mater Sci: Mater Electron (2017) 28:7029–7035
DOI 10.1007/s10854-016-6077-x

Low temperature micro Raman and laser induced upconversion and downconversion spectra of europium doped silver tungstate $Ag_{2-3x}Eu_xWO_4$ nanorods

Ivo M. Pinatti[1,2] · Terry G. Ireland[1] · George R. Fern[1] · Ieda L. V. Rosa[2] · Jack Silver[1]

Received: 30 August 2016 / Accepted: 11 November 2016 / Published online: 3 December 2016

Abstract All the red emitting europium-doped silver tungstate α-$Ag_{2-3x}Eu_xWO_4$ (x = 0.01–0.08 mol) phosphor reported herein crystalise as nanorods. The nanorods were structurally characterised by X-ray powder diffraction, Rietveld refinement, low temperature (20 to −190 °C) micro-Raman spectroscopy . The morphology of the nanorods reported herein was confirmed by field emission scanning electron microscopy. The optical properties were studied using low temperature (20 to −190 °C) high resolution laser excited upconversion and downconversion luminescence.

1 Introduction

Although there are several ways of producing white light from blue light emitting diodes, LEDs, the preferred way for good colour rendering involves the use of green and red emitting conversion phosphors [1]. Recently, many Eu^{3+}-doped tungstate based lattices (as host for the Eu^{3+} activators that emit the red light) have been reported for possible application as red conversion phosphors examples include $CdWO_4$ [2, 3], $SrWO_4$ [4, 5], Y_6WO_{12} [6], $KLa(WO_4)_2$ [7], $RbGd(WO_4)_2$ [8], $NaY(WO_4)_2$ [9], $NaGd(WO_4)_2$ [10], $Na_2Dy_4(WO_4)_7$ [11], $La_2W_2O_9$ [12], $ZnWO_4$ [13], $Ba_4Na_2W_2O_{11}$ [14], $MgWO_4$ [15], and $Li_2Mg_2(WO_4)_3$ [16]. Some of these materials require high amounts of the expensive europium activator. However, it is notable that due to the price and critical resource of rare earth elements, it would be better to reduce the amount of these elements for an economic, energetic and environmental friendly synthesis procedure.

The emission characteristic of a material strongly depends on the crystal structure of the host lattice as well as its uniformity, doping sites and the doping concentration of the activator that is emitting. Considering the doping sites, characteristics such as distance between dopants, coordinate numbers, relative spatial position and electrical environments are also important in order to fully understand the photoluminescence properties [17]. Many tungstate lattices when acting as hosts for Eu^{3+} activators have been shown to manifest excellent luminescent efficiency and color purity as well as having high average refractive indexes [2–16]. Also this class of tungsten oxides can be considered as ideal host lattices for dopants as they possess high thermal, chemical and physical stability and in addition they can often be synthesized at low temperatures. They also have broad and intense ligand-to-metal charge transfer (LMCT) band(s) in the UV or near-UV region that are able to capture the emission from an InGaN-based LED.

The α-Ag_2WO_4 lattice is the host lattice chosen for the work reported herein. The crystal symmetry of the α-Ag_2WO_4 lattice is orthorhombic, and the space group is *Pn2n* [18]. Each W atom is bonded to six oxygen atoms and the Ag^+ cations are found to have two, four, six and seven-coordinated geometry. Both WO_6 and AgO_6 cluster have site symmetry of O_h and AgO_2, AgO_4 and AgO_7 polyhedra have site symmetry of C_{2v}, T_d and D_{5h}, respectively. In fact the Ag^+ cation content in the four different coordination sites in α-Ag_2WO_4 differ dramatically, 15% of these sites are non-centro-symmetric with C_{2v} symmetry (AgO_2), 37% are non-centro-symmetric with

✉ Terry G. Ireland
terry.ireland@brunel.ac.uk

[1] Wolfon Centre for Materials Processing, Brunel University London, Kingston Lane, Uxbridge, Middlesex UB8 3PH, UK

[2] INCTMN, LIEC, Chemistry Department, Federal University of São Carlos, P.O. Box 676, São Carlos, SP 13565, Brazil

T_d symmetry (AgO_4), 18% are centro-symmetric with O_h symmetry (AgO_6) and 30% are non-centro-symmetric with D_{5h} symmetry (AgO_7) [18–20]. Thus, the electric dipole $^5D_0 \rightarrow {}^7F_2$ transition in the reported spectra is caused specifically by the Eu^{3+} located at one or more of the non-centro symmetric sites [21].

A range of applications for silver tungstate is reported in the literature these include chemical fixation of CO_2 [22], a catalyst in organic chemistry [23], photoswitches [24], photocatalysis of organic pollutants [25–30], lubricants [31], electrocatalysis [32], gas sensor [33, 34], LED [35] as well as an antimicrobial and antibacterial agents [36–38]. The influence of electron beam irradiation on structural and optical properties of this material has also been investigated [39]. A further interesting potential future application is in the field of laser refrigeration of nanocrystals [40, 41].

Previously it was reported that the red emitting europium doped silver tungstate α-$Ag_{2-3x}Eu_xWO_4$ ($x = 0.0$–0.01 mol) phosphor crystalises as nanorods and it was suggested that it could be used for blue LED colour conversion as the red emitter for white light, however in the Eu^{3+} concentrations studied it was not bright enough for the application [21]. Thus in this work we report on attempts to increase the Eu^{3+} concentration in red emitting europium doped silver tungstate α-$Ag_{2-3x}Eu_xWO_4$ ($x = 0.01$–0.08 mol%) phosphor report to further assess its potential for use in new applications based on its' nano-rod morphology which allows for preferred alignment, dense packing and directional emission characteristics. These Eu^{3+} concentrations are much smaller than tungstate lattices such as $LiEu(WO_4)_2$ which have been suggested as candidates for red emitting LED phosphors [35].

2 Experimental

The nanorods were synthesised via a low temperature (90 °C) coprecipitation route [21]; the nanorods emitted red light without further heat treatments.

The nanorods were structurally characterised by X-ray powder diffraction, Rietveld refinement, low temperature (20 to −190 °C) micro-Raman spectroscopy. The latter allows enhanced spectroscopic analysis of materials; Raman spectra can be collected from areas down to 1 μm^2. Allowing the selective identification of structural and chemical differences in inhomogeneous samples or single particles. Combined with automated focusing using a XYZ stage three-dimensional chemical imaging is possible focusing below the surface of the sample. It is also possible to observe damage to the sample by the laser during measurement. In our case we were able to focus on small groups of nanorods and did not damage them. The morphology of the nanorods was confirmed by field emission scanning electron microscopy (FESEM).

3 Results

Figure 1 presents the X-ray powder diffraction (XRD) patterns of α-$(Ag_{2-3x}Eu_x)WO_4$ samples. All of the peaks observed in the patterns can be indexed to the pure orthorhombic phase of α-Ag_2WO_4 and are in good accordance with PDF no 34-0061. These results indicate that Eu^{3+} cations have been introduced efficiently into the α-Ag_2WO_4 lattice until 4 mol% Eu^{3+}. For 8 mol% Eu^{3+} it is possible to observe small peaks related to Silver Europium Tungsten Oxide (PDF no 60-0818) at 27.80°, 28.5° and 29.8° indicated with "*" in Fig. 1. This is evidence of saturation of the α-Ag_2WO_4 orthorhombic structure by the Eu^{3+} cations.

The substitution of monovalent Ag^+ cations by trivalent Eu^{3+} cations will cause strain in the lattice. This is because for every Eu^{3+} cation occupying an Ag^+ cation site two more Ag^+ cations have been displaced from the lattice leaving two cation vacancies, Ag_v^+ this maintains charge

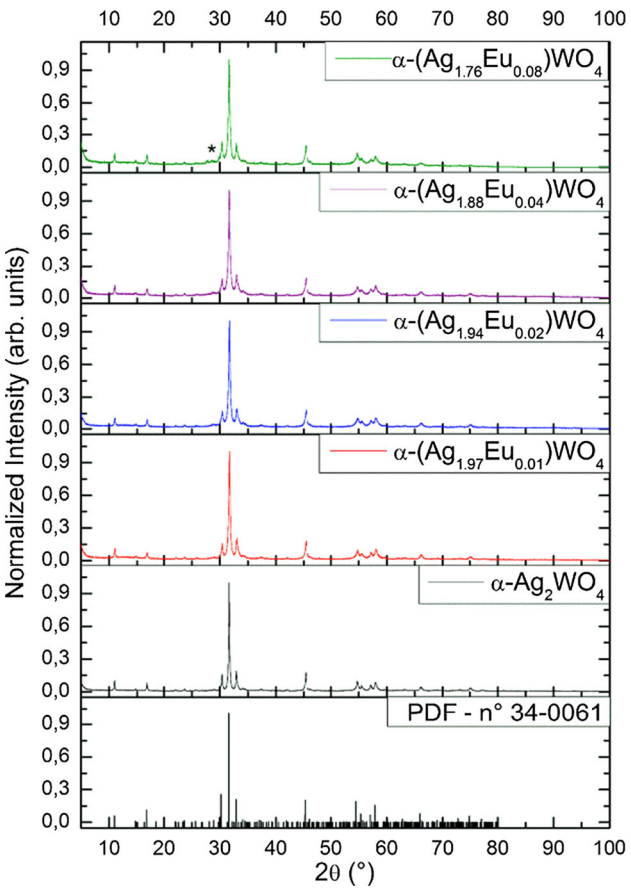

Fig. 1 XRD pattern of the samples α-$(Ag_{2-3x}Eu_x)WO_4$ ($x = 0$–8 mol%)

compensation in the lattice but both the vacancies and the 3^+ charged cations cause strain as can be seen from the fact that as the proportion of the Eu^{3+} cations is increased the Eu^{3+} cations are rejected from occupying the vacant sites. This means that in the α-$(Ag_{2-3x}Eu_x)WO_4$ structure x cannot be tolerated much above 0.04 Mol%. So, in this lattice charge compensation can only be tolerated to a small extent. In fact at 0.04mol% Eu^{3+} 0.12mol% of Ag+ cations have been removed (that is around one in eight of the Ag^+ cations present. Though the ionic radius of Ag^+ is 1.22 Å, and that of Eu^{3+} is 1.087 Å the latter will tend to distort the crystal site normally occupied by the former because of its greater charge [42–44]. The synthetic conditions would not favour Eu^{2+} formation (reducing conditions would be required), if Eu^{2+} was present it would be observed as a broad peak in the photoluminescence spectrum.

Structural refinement data of the α-$(Ag_{2-3x}Eu_x)WO_4$ (x = 0.0–0.08) samples confirm the orthorhombic structure with a *Pn2n* symmetry space group. The experimental lattice parameters and unit cell volumes calculated using the Rietveld refinement method are shown in Table 1. This table shows low deviations of statistical parameters (weighted profile R-factor (R_{wp}), expected R-factor (R_{exp}), residual of least-squares refinement (R_p) and reflection intensity-based R-factors (R_{Bragg}) which suggests that the refinement results are quite reliable and with good numerical results. These results were obtained by keeping the occupancy of W^{6+} fixed to 1 while Eu^{3+} cations were set to share occupancies in the Ag^+ sites.

The size distribution and morphology of the crystals are important parameters in both luminous flux and their ordering on a surface (for device application). For many applications it would be ideal to have uniform sub-micron phosphor particles without any reduction in the luminous efficacy (compared to larger micron sized particles.

In Fig. 2a–d FESEM micrographs of the samples are presented. It is possible to see clear boundaries between the crystals indicating that there is no strong adhesion among the crystals. Moreover, there are in all cases many crystals of similar size and shape showing no evidence of aggregation, nor formation of larger structures. Most of the crystals are smooth surfaced nanorods of around 100 nm in width and 1–2 μm in length. The nanorod morphology should facilitate preferential alignment, dense packing and directional emission characteristics.

The Raman spectra of the phosphors may be useful for obtaining information about parameters which affect the luminescence efficiency. These parameters include crystallographic phases, lattice phonon energies, and the site symmetries of activators [45]. As α-Ag_2WO_4 belongs to the C_{2v}^{10} point group and has two molecular formulas per unit cell (Z = 2). Group theory predicts that there are 21 different Raman modes [46], of these 14 modes have previously been identified [21].

Figures 3 and 4 present the room temperature Raman spectra of the α-$(Ag_{2-3x}Eu_x)WO_4$ (x = 0–0.08 mol) samples excited at 532 and 633 nm, respectively. These spectra are very similar to those reported and assigned for the α-$Ag_{2-3x}Eu_xWO_4$ (x = 0.0–0.01 mol) phosphor samples [21]. The differences in the Raman spectra presented in Figs. 3 and 4 and those presented in reference 21 are due to the presence of some luminescence (emission bands from the larger concentrations of Eu^{3+} present in the samples studied in this work, we will present evidence for this in later Figures and discuss this more below. The Raman modes and their respectively assignments are shown in the Figures. The Raman modes below 251 cm^{-1} are related to the translational lattice vibrations of Ag^+ and W^{6+}, mainly contributed by the motion of heavy Ag^+ ions. The out of plane bending modes of WOOW are observed at 306 cm^{-1}. The modes at 340 and 367 cm^{-1} are due to the bending vibrations of O–W–O, WOOW, and W–O–W. The modes at 489 and 510 cm^{-1} are related to the out of plane wagging of WOOW. The mode at 589 cm^{-1} is the bending vibrations of W–O–W and WOOW. The mode at 666 cm^{-1} is due to the stretching modes of WOOW. The modes at 749 and 779 cm^{-1} result from the symmetric stretching modes of WOOW and W–O. The mode at 805 cm^{-1} arises from the asymmetric stretching modes of

Table 1 Lattice parameters, unit cell volume and statistical parameters of quality

A-$(Ag_{2-3}Eu_x)WO_4$	Lattice paramaters (Å)			Cell volume ($Å^3$)	R_{exp} (%)	R_{wp} (%)	R_p (%)	R_{Bragg} (%)	Crystal size (nm)
	a	b	c						
x = 0	10.8799 (3)	12.0164 (5)	5.8911 (2)	770.19 (5)	7.53	16.0	12.36	6.380	32.98 (16)
x = 0.01	10.875 (4)	12.064 (4)	5.889 (2)	771.3 (5)	7.15	14.90	11.17	6.349	22.84 (16)
x = 0.02	10.867 (3)	12.026 (4)	5.8956 (18)	770.5 (4)	7.15	11.90	9.29	3.809	19.31 (10)
x = 0.04	10.8635 (9)	12.024 (11)	5.8979 (6)	770.45 (12)	7.00	11.94	9.38	4.077	18.25 (11)
x = 0.08	10.857 (7)	12.012 (7)	5.902 (4)	769.7 (8)	7.53	16.00	12.59	7.076	29 (2)

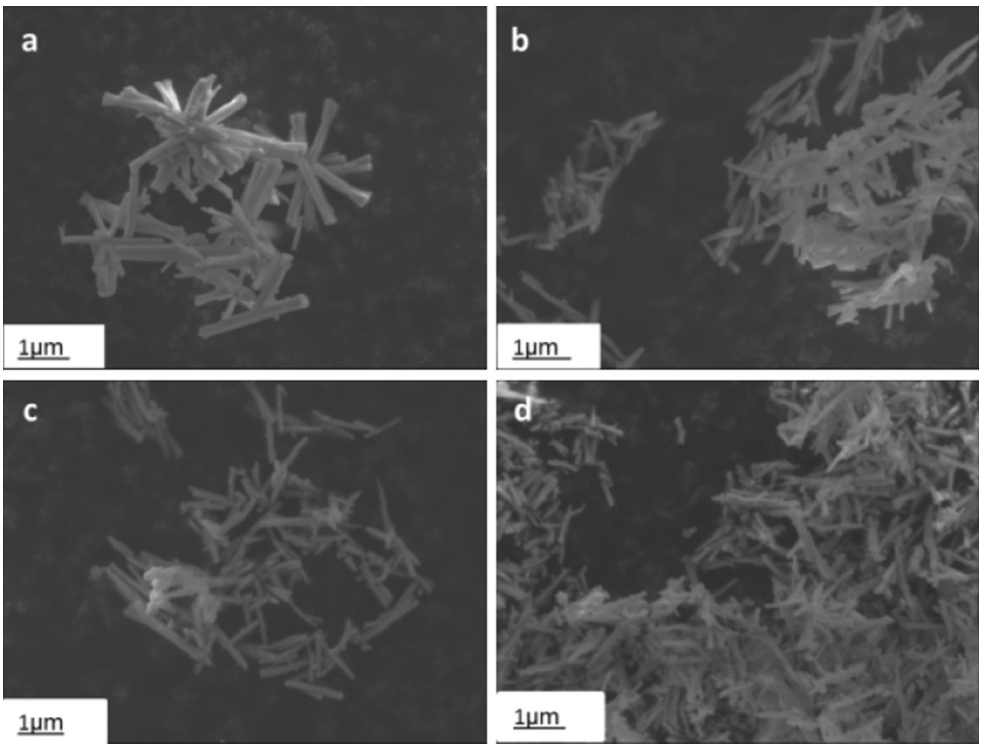

Fig. 2 FESEM micrographs of samples α-$(Ag_{2-3x}Eu_x)WO_4$. **a** x = 0; **b** x = 0.01; **c** x = 0.02; **d** x = 0.04

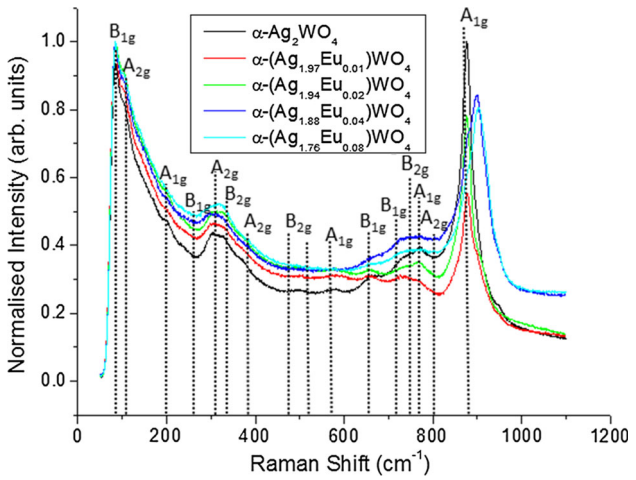

Fig. 3 Raman spectra of the samples α-$(Ag_{2-3x}Eu_x)WO_4$ (x = 0–0.08 mol) excited at 532 nm

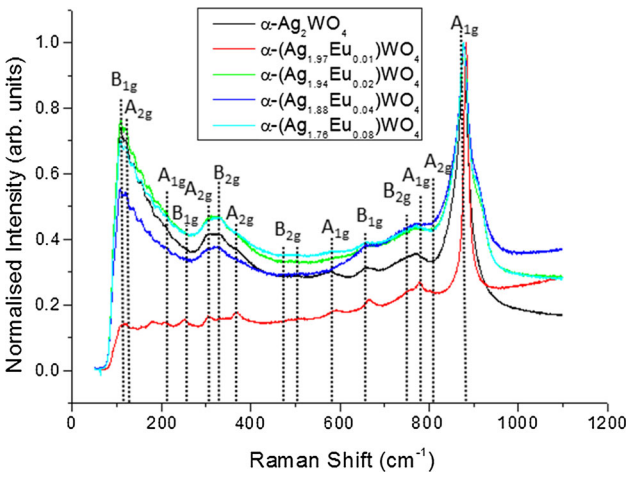

Fig. 4 Raman spectra of the samples α-$(Ag_{2-3x}Eu_x)WO_4$ (x = 0–8 mol%) excited at 633 nm

W–O–W and W–O and the mode observed at 883 cm^{-1} is from the symmetric stretching of W–O [47].

The main features observed are for samples with x > 2 mol% (λ_{exc} = 532 nm), in which the mode A_{1g} at 883 cm^{-1} appears to shifts to higher wavenumber because of the this is because of an underlying emission band that gets stronger and causes the apparent movement of the Raman band as the Eu^{2+} concentration increases in the α-Ag_2WO_4 lattice. These underlying emission bands also affect the spectra collected with the 633 nm laser line (Fig. 4), saturation also causes broadening of the bands as observed on the spectra excited at 633 nm. However in the latter case these emission bands are less intense and so only a broadening is observed that becomes a shoulder at the higher Eu^{3+} concentrations.

In Figs. 5 and 6 the room temperature Anti-Stokes and Stokes luminescence and Raman spectra of the α-$(Ag_{2-3x}Eu_x)WO_4$ (x = 0–0.08 mol%) samples excited at 532 and 633 nm are presented. In the case of the spectra excited at 633 nm (Fig. 6) the emission bands at higher energy are

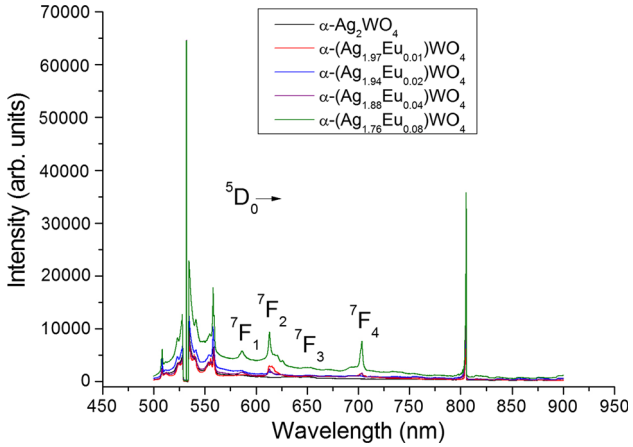

Fig. 5 PL-Raman spectra of the samples α-$(Ag_{2-3x}Eu_x)WO_4$ (x = 0 – 0.08 mol) excited at 532 nm

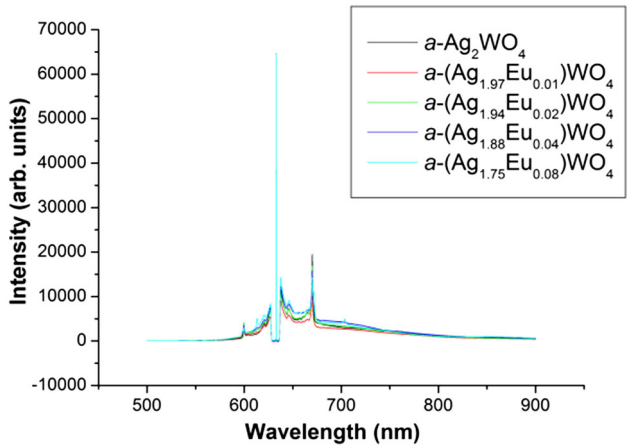

Fig. 6 PL-Raman spectra of the samples α-$(Ag_{2-3x}Eu_x)WO_4$ (x = 0–0.08 mol) excited at 633 nm

observed due to a combination of the energy of the laser line plus the thermal energy of the electrons in the ^7F_j states [48]. For the 532 nm excited spectra the higher energy emission bands may arise from a similar process or alternatively (but less likely) they may be excited by a two photon upconversion process. The strongest Raman modes typical of α-Ag_2WO_4 are seen on both anti-Stokes and Stokes sides of the spectra. The characteristic emission bands seen in Figs. 5 and 6 at around 591, 616, 652 and 702 nm are due to the $^5D_0 \rightarrow {}^7F_1$, $^5D_0 \rightarrow {}^7F_2$, $^5D_0 \rightarrow {}^7F_3$ and $^5D_0 \rightarrow {}^7F_4$ transitions, respectively [48].

The temperature dependence of the Raman spectra of α-$(Ag_{1.97}Eu_{0.01})WO_4$ excited at 633 nm is presented in Fig. 7. These spectra show that as the temperature decreases, improvement of the Raman modes definition occurs due to less lattice vibrations (thermal energy) at lower temperatures depopulating the luminescence spectra [48]. Thus the broad emission bands seen below 550 cm^{-1}

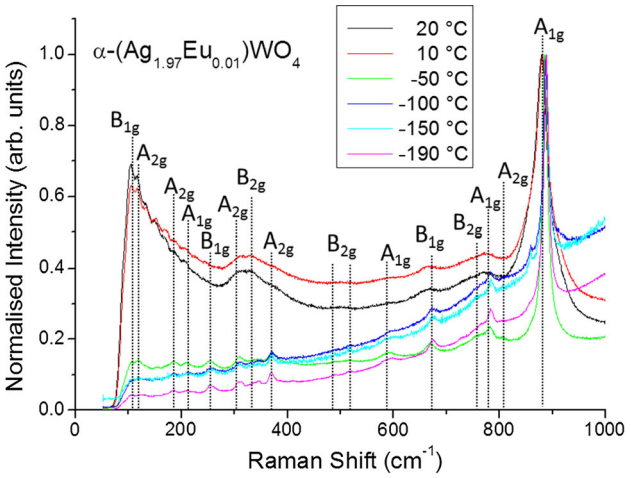

Fig. 7 Temperature-dependent Raman spectra of α-$(Ag_{1.97}Eu_{0.01})WO_4$ excited at 633 nm

in the 20 and 10 °C spectra in Fig. 5 are not present in the −50 °C spectrum.

The temperature dependence of the Stokes and anti-Stokes emission spectra of α-$(Ag_{1.95}Eu_{0.01})WO_4$ excited at 633 nm is presented in Fig. 8. These spectra indicate that the intensities of all of the anti-Stokes and Stokes luminescence lines manifest temperature-dependent behavior (losing intensity as the temperature decreases) in line with the fact that less energy is available to thermally populate the $^7F_0$, $^7F_1$, $^7F_2$, $^7F_3$ and $^7F_4$ states of Eu^{3+} at the lower temperatures [48]. It is apparent that as the temperature decreases to −190 °C the only remaining bands on the low energy side in Fig. 6 are the Raman bands. It is apparent from Fig. 8 that the emission bands are no longer present at −100 °C.

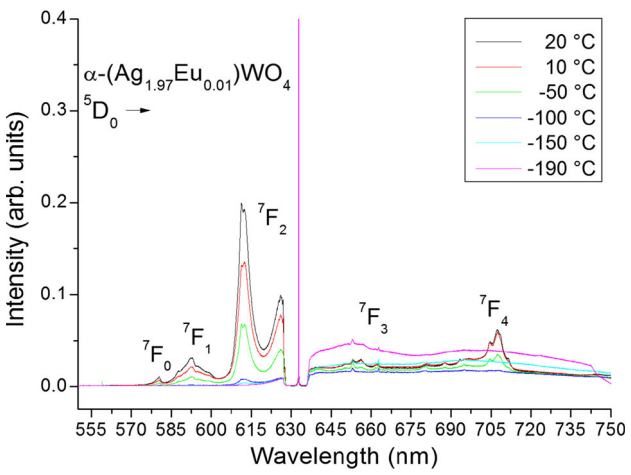

Fig. 8 Temperature-dependent PL-Raman spectra of α-$(Ag_{1.97}Eu_{0.01})WO_4$ excited at 633 nm

4 Conclusions

This work demonstrated that nanometre-sized α-($Ag_{2-3x-y}Eu_xLi_y$) WO_4 crystals were efficiently prepared by the coprecipitation method without further treatments. XRD and Rietveld analysis confirmed the phase and the lattice parameters of each doping concentration. FESEM studies revealed nanorods of around 1 μm in length and 100 nm in width which allows preferred alignment, dense packing and directional emission characteristics. Using the 633 nm laser to study the Raman spectra also allowed the optical properties to be partially studied using low temperature (20 to −190 °C) high resolution laser excited upconversion and downconversion luminescence. It is apparent from this work that as the temperature was lowered the emission bands became less intense and eventually disappear, showing they are only seen via upconversion due to thermal population of the ground state of the Eu3+ ions in the lattice. The excitation spectra showed excitation maxima at 395 and 465 nm which are in the ideal regions for excitation by both UV and blue LEDs; these bands were determined by monitoring the main Eu^{3+} emission peak at 615 nm. Emission spectra showed red emission at 615 nm showing the potential for use as colour converting phosphors for use with the LEDs. A fuller study of the excitation and emission spectra of these materials will be published separately.

Acknowledgements We are grateful to the EPSRC and Technology Strategy Board (TSB) for funding the PURPOSE (TP11/MFE/6/1/AA129F; EP-SRC TS/G000271/1) and CONVERTED (JeS no. TS/1003053/1), PRISM (EP/N508974/1) and FAB3D programs. We are also grateful to the TSB for funding the CONVERT program. The authors also appreciate the support of FAPESP (São Paulo Research Foundation, Grant#2013/07296-2, Grant#2013/23995-8 and Grant#2015/13669-1).

References

1. J. Silver, R. Withnall, *Colour Conversion Phosphors for LEDs" in Luminescent Materials and Applications* (Wiley, Weinheim, 2008)
2. J. Lin, J. Yang, J. Gao, Q. Wang, Polyhedron **113**, 102–108 (2016)
3. W.J. Zhang, W.L. Feng, Y.M. Nie, Optik **126**, 1341–1343 (2015)
4. S.K. Gupta, K. Sudarshan, P.S. Ghosh, K. Sanyal, A.P. Srivastava, A. Arya, P.K. Pujari, R.M. Kadam, RSC. Adv. **6**, 3792–3805 (2016)
5. B.P. Maheshwary, R.A. Singh, Spectrochim. Acta–A Mol. Biomol. Spectrosc. **152**, 199–207 (2016)
6. T.C. Chien, J.C. Yang, C.S. Hwang, M. Yoshimura, J. Alloys Compd. **676**, 286–291 (2016)
7. K.K. Rasu, D. Balaji, S.M. Babu, J. Lumin. **170**, 547–555 (2016)
8. K.K. Rasu, D. Balaji, S.M. Babu, J. Lumin. **170**, 825–834 (2016)
9. T. Liu, Q. Meng, W. Sun, J. Lumin. **170**, 219–225 (2016)
10. Y. Wang, J. Tang, X. Huang, L. Jiang, J. Rare Earths **34**, 118–124 (2016)
11. W. Zhang, C. Yuan, R. Hua, T. Liu, K. Song, J. Yu, D. Tang, Y. Gao, B. Chen, J. Nanosci. Nanotechnol. **16**, 822–827 (2016)
12. K. Song, G.M. Li, J. Mater. Sci. Mater-El. **27**, 1227–1231 (2015)
13. Y. Zhai, M. Wang, Q. Zhao, J. Yu, X. Li, J. Lumin. **172**, 161–167 (2016)
14. X. Qiao, S. Qi, Y. Lu, Y. Pu, Y. Huang, X. Wang, J. Alloys Compd. **656**, 189–195 (2016)
15. X. Feng, W. Feng, M. Xia, K. Wang, H. Liu, D. Deng, X. Qin, W. Yao, W. Zhu, RSC Adv. **6**, 14826–14831 (2016)
16. H. Zhu, M. Fang, Z. Huang, Y.G. Liu, K. Chen, X. Min, Y. Mao, M. Wang, J. Lumin. **172**, 180–184 (2016)
17. C. Chen, C. Li, Z. Si, Adv. Sci. **3**, 1600029 (2016)
18. P.M. Skarstad, S. Geller, Mater. Res. Bull. **10**, 791–799 (1975)
19. L.S. Cavalcante, M.A.P. Almeida, W. Avansi Jr., R.L. Tranquilin, E. Longo, N.C. Batista, V.R. Mastelaro, M.S. Li, Inorg. Chem. **51**, 10675–10687 (2012)
20. J. André, L. Gracia, P. Gonzalez-Navarrete, V.M. Longo, W. Avansi Jr., D.P. Volanti, M.M. Ferrer, P.S. Lemos, F.A. La Porta, A.C. Hernandes, E. Longo, Sci. Rep. **4**, 5391–5397 (2014)
21. I.M. Pinatti, I.C. Nogueira, W.S. Pereira, P.F.S. Pereira, R.S. Gonçalves, J.A. Varela, E. Longo, L.V. Rosa, Dalton Trans. **44**, 17673–17685 (2015)
22. Q.W. Song, B. Yu, X.D. Li, R. Ma, Z.F. Diao, R.G. Li, W. Li, L.N. Li, Green Chem. **16**, 1633–1638 (2014)
23. C.X. Guo, B. Yu, J.N. Xie, L.N. He, Green Chem. **17**, 474–479 (2014)
24. L. Cheng, Q. Shao, M. Shao, X. Wei, Z. Wu, J. Phys. Chem. C **113**, 1764–1768 (2009)
25. R. Zhang, H. Cui, X. Yang, H. Liu, H. Tang, Y. Li, Micro & Nano Lett. **7**, 1285–1288 (2012)
26. X. Liu, J. Hu, J. Li, Y. Hu, Y. Shao, H. Yang, G. Tong, H. Qian, Mater. Lett. **91**, 129–132 (2013)
27. H. Chen, Y. Xu, Appl. Surf. Sci. **319**, 319–323 (2014)
28. J. Tang, J. Ye, J. Mater. Chem. **15**, 4246–4251 (2005)
29. X. Wang, C. Fu, P. Wang, H. Yu, J. Yu, Nanotechnology **24**, 165602 (2013)
30. Z. Lin, J. Li, Z. Zheng, J. Yan, P. Liu, C. Wang, G. Yang, ACS Nano **9**, 7256–7265 (2015)
31. D. Stone, J. Liu, D.P. Singh, C. Muratore, A.A. Voevodin, S. Mishra, C. Rebholz, Q. Ge, S. Aquadi, Scr. Mater. **62**, 735–738 (2010)
32. L. Pan, L. Li, Y. Chen, J. Sol-Gel. Sci. Technol. **66**, 330–336 (2013)
33. L.F. Da Silva, A.C. Catto, W. Avansi Jr., L.S. Cavalcante, J. Andres, K. Aguir, V.R. Mastelaro, E. Longo, Nanoscale **6**, 4058–4062 (2014)
34. L.F. Da Silva, A.C. Catto, W. Avansi, L.S. Cavalcante, V.R. Mastelaro, J. Andres, K. Aguir, E. Longo, J. Alloys Compd. **683**, 186–190 (2016)
35. A. Sreedevi, K.P. Priyanka, S.R. Mary, E.M. Mohammed, T. Varghese, Adv. Sci. Eng. Med. **7**, 498–505 (2015)
36. Q. Wang, X. Guo, W. Wu, S. Liu, Adv. Mater. Res. **284–286**, 1321–1325 (2011)
37. D.P. Dutta, A. Singh, A. Ballal, A.K. Tyagi, Eur. J. Inorg. Chem. **2014**, 5724–5732 (2014)
38. V.M. Longo, C.C. De Foggi, M.M. Ferrer, A.F. Gouveia, R.S. Andre, W. Avansi, C.E. Vergani, A.L. Machado, J. Andres, L.S.

Cavalcante, A.C. Hernandes, E. Longo, J. Phys. Chem. A **118**, 5769–5778 (2014)
39. A. Sreedevi, K.P. Priyanka, K.K. Babitha, S. Ganesh, T. Varghese, Micron **88**, 1–6 (2016)
40. P.B. Roder, B.E. Smith, X. Zhou, M.J. Crane, P.J. Pauzauskie, PNAS **112**, 15024–15029 (2015)
41. X. Zhou, B.E. Smith, P.B. Roder, P.J. Pauzauskie, Adv. Mater. **28**, 8658–8662 (2016). doi:10.1002/adma.201600406
42. X. Yan, G.R. Fern, R. Withnall, J. Silver, J. Nanoscale **5**, 1091–1096 (2013)
43. M. Pulchalska, E. Zych, M. Sobczyk, A. Watras, P. Deren, Mater. Chem. Phys. **147**, 304–310 (2014)
44. R.D. Shannon, Acta Cryst. **A32**, 751–767 (1976)
45. J. Silver, R. Withnall, Chem. Rev. **104**, 2833–2856 (2004)
46. A. Turkovic, D.L. Fox, J.F. Scott, Mat. Res. Bull. **12**, 189–195 (1977)
47. H.H. Xi, D. Zhou, H.D. Xie, B. He, Q.P. Wang, N. Alford, J. Am. Ceram. Soc. **98**, 587–593 (2015)
48. J. Silver, M.I. Martinez-Rubio, T.G. Ireland, G.R. Fern, R. Withnall, J. Phys. Chem. B. **105**, 948–953 (2001)